



Article

# Research on Thermal Runaway Characteristics of High-Capacity Lithium Iron Phosphate Batteries for Electric Vehicles

Qing Zhu, Kunfeng Liang \* and Xun Zhou

Vehicle and Traffic Engineering College, Henan University of Science and Technology, Luoyang 471003, China; 210321030259@stu.haust.edu.cn (Q.Z.); xunzhou@haust.edu.cn (X.Z.)

\* Correspondence: lkf@haust.edu.cn

**Abstract:** With the rapid development of the electric vehicle industry, the widespread utilization of lithium-ion batteries has made it imperative to address their safety issues. This paper focuses on the thermal safety concerns associated with lithium-ion batteries during usage by specifically investigating high-capacity lithium iron phosphate batteries. To this end, thermal runaway (TR) experiments were conducted to investigate the temperature characteristics on the battery surface during TR, as well as the changes in battery mass and expansion rate before and after TR. Meanwhile, by constructing a TR simulation model tailored to lithium iron phosphate batteries, an analysis was performed to explore the variations in internal material content, the proportion of heat generation from each exothermic reaction, and the influence of the heat transfer coefficient during the TR process. The results indicate that as the heating power increases, the response time of lithium-ion batteries to TR advances. Furthermore, the heat released from the negative electrode–electrolyte reaction emerges as the primary heat source throughout the entire TR process, contributing to 63.1% of the total heat generation.

**Keywords:** lithium iron phosphate batteries; thermal safety; thermal runaway; temperature characteristics; electric vehicle



**Citation:** Zhu, Q.; Liang, K.; Zhou, X. Research on Thermal Runaway Characteristics of High-Capacity Lithium Iron Phosphate Batteries for Electric Vehicles. *World Electr. Veh. J.* **2024**, *15*, 147. <https://doi.org/10.3390/wevj15040147>

Academic Editor: Joeri Van Mierlo

Received: 4 March 2024

Revised: 23 March 2024

Accepted: 30 March 2024

Published: 3 April 2024



**Copyright:** © 2024 by the authors. Licensee MDPI, Basel, Switzerland. This article is an open access article distributed under the terms and conditions of the Creative Commons Attribution (CC BY) license (<https://creativecommons.org/licenses/by/4.0/>).

## 1. Introduction

As the promotion of carbon peaking and carbon neutrality gains momentum, expediting the completion of technological upgrades in the new energy vehicle industry has emerged as an urgent issue for many countries. When it comes to reducing carbon emissions, pure electric vehicles offer unparalleled advantages over traditional fuel vehicles. In pure electric vehicles, batteries serve as the power source [1–4], playing a critical role in determining the driving range. However, in recent years, the safety concerns associated with battery thermal runaway incidents in pure electric vehicles have received widespread attention due to frequent occurrences of explosive combustion incidents. Consequently, preventing or mitigating the risk of lithium-ion battery thermal safety accidents has become a paramount concern for both the automotive and battery industries [5,6].

Currently, ternary lithium-ion batteries and lithium iron phosphate batteries are the commonly used types of batteries in electric vehicles. Lithium iron phosphate batteries are more widely used in public transportation. Although they exhibit slightly better thermal stability compared to ternary lithium-ion batteries, their thermal safety concerns cannot be ignored. Numerous scholars have conducted experiments and simulation studies to investigate the thermal safety of lithium-ion batteries. In a study by Zhou et al. [7], the thermal runaway (TR) of lithium iron phosphate batteries was investigated by comparing the effects of bottom heating and frontal heating. The results revealed that bottom heating accelerates the propagation speed of internal TR, resulting in higher peak temperatures and increased heat generation. Wang et al. [8] examined the impact of the charging rate on the TR of lithium iron phosphate batteries. They found that as the charging rate increases,

the growth rate of lithium dendrites also accelerates, leading to microshort circuits and subsequently increasing the TR occurrence of lithium iron phosphate batteries. The effects of different heating positions, including large surface heating, side heating, and bottom heating, on the TR of lithium iron phosphate batteries were compared by Huang et al. [9]. It was observed that large surface heating produces the maximum smoke volume, jet velocity, and jet duration during the TR process. Zhao et al. [10] induced TR in ternary lithium-ion batteries through localized heating and studied the variation of internal thermal characteristics under different cooling conditions. When comparing the performance of lithium-ion batteries with different positive electrode materials during TR, Wang et al. [11] demonstrated that lithium iron phosphate batteries release a large amount of smoke during TR and exhibit poor overcharge tolerance. On the other hand, ternary lithium-ion batteries show better performance in terms of energy density and overcharge tolerance but may experience explosions during TR. Feng et al. [1,12,13] utilized EV-ARC to investigate the TR mechanism and characteristics of large-capacity ternary lithium-ion batteries. An adiabatic TR experiment with sudden cessation was designed, and the cooled batteries' life decay mechanism was analyzed, revealing the thermo-electric coupling mechanism during the adiabatic TR test process of lithium-ion power batteries. Li et al. [14] conducted experiments by heating the surface and interior of lithium iron phosphate batteries using a heater to study the effects of different heating positions on the TR of lithium-ion batteries. The results showed that when the heater was external, there was a significant delay in the first stage of TR, but the maximum temperature and mass loss of the battery during TR were higher compared to when the heater was internally propagating inside the lithium-ion battery. Huang et al. [15] performed thermal chamber tests on ternary lithium-ion batteries at different states of charge, comprehensively studying characteristics such as the self-heat decomposition temperature and voltage change component transition of lithium-ion batteries during TR. The results indicated that as the state of charge increased from 0% to 100%, the critical temperature for lithium-ion battery TR decreased by 40 °C. During TR, the positive electrode material dissolved into small particles, and the surface became uneven. Liu et al. [16] investigated the effects of two different triggering methods, overheating and overcharging, on the TR of lithium iron phosphate batteries. Their findings demonstrated that under overcharge conditions, battery combustion is more severe, leading to higher fire risks.

Experimental studies on the thermal runaway (TR) of lithium-ion batteries have shown low repeatability and involve certain risks, requiring significant human and material resources. Furthermore, these studies are economically inefficient as they only provide limited observations of surface phenomena during the experimental process. In order to overcome these limitations, researchers have turned to numerical simulation software to simulate the thermal runaway process of lithium-ion batteries. This approach allows for accurate observations of temperature variations within the battery at different time intervals. As a result, an increasing number of scholars are engaging in in-depth research in this field. Ren et al. [17–19] conducted a study that combined an electrochemical–thermal coupled model with a thermal abuse model to predict the thermal behavior of lithium-ion batteries during overcharging. The results demonstrated that increasing the onset temperature of thermal runaway can effectively improve the performance of overcharging. Jin et al. [20] developed a three-dimensional simulation model to investigate the comprehensive effects of heating area and heating power on the thermal runaway of lithium-ion batteries. They found that smaller heating areas and higher heating powers result in faster triggering of thermal runaway. Zhang et al. [21], focusing on lithium iron phosphate batteries, analyzed the differences in data observed during thermal runaway under differential scanning calorimetry (DSC) and Accelerating Rate Calorimetry (ARC) testing conditions. Their analysis provided an effective dataset for thermal runaway modeling. Rojo et al. [22] replaced the battery failure location with a cylinder to study the spreading behavior of thermal runaway in lithium-ion batteries. They explored the influence of external laminar and turbulent flow conditions on thermal runaway by establishing a simulation model.

Antonio et al. [23] compared thermal runaway models of batteries with different cathode materials and analyzed the differences in reaction mechanisms during the thermal runaway process. Xu et al. [24] proposed a thermal runaway propagation model that improves model-solving speed by coupling reduced-order thermal and thermal runaway models at the mini module, real module, and pack levels.

Some scholars have also conducted a certain amount of research on gas evolution, preventive measures, and other issues related to the TR process of lithium-ion batteries. Jin et al. [25], Koch et al. [26], and Wang et al. [27] analyzed thermal runaway, gas generation types, and contents under overheat and overcharge conditions for lithium iron phosphate batteries. Huang et al. [28] investigated the effect of series and parallel connections between batteries on thermal runaway. They found that the propagation speed of thermal runaway in lithium-ion batteries is accelerated under parallel conditions. Yu et al. [29] and Xiao et al. [30] studied the influence of different insulation materials and thicknesses on the propagation of thermal runaway using various thermal insulation materials between lithium iron phosphate batteries. Hang et al. [31] explored the inhibitory and delaying effects of liquid nitrogen on lithium-ion battery thermal runaway. Their research revealed that the delaying effect of liquid nitrogen on thermal runaway decreases as the battery surface temperature increases. Lie et al. [32,33] and others studied the inhibitory effects of immersion cooling on battery thermal runaway under different charge and discharge conditions.

At present, although some conclusions and experimental results have been achieved in the research on TR of lithium-ion batteries, studying the internal mechanism changes during the TR process of lithium-ion batteries remains a challenging issue faced by the industry. The internal heat generation within the battery during TR cannot be effectively expressed through experimental methods. By establishing reliable TR models for lithium-ion batteries, the internal temperature changes and heat generation changes during TR can be more intuitively expressed. This aids in better understanding the trends and patterns of lithium-ion battery TR, enabling the adoption of preventive measures in advance to reduce potential risks. This holds extremely significant implications for guiding lithium-ion battery safety.

Lithium-ion battery TR is primarily triggered by three types of abuse [1,34]: electrical abuse, thermal abuse, and mechanical abuse. Among these, thermal abuse is one of the primary methods for inducing TR in lithium-ion batteries and is widely applied in lithium-ion battery thermal safety research. This paper builds on previous studies by specifically focusing on exploring thermal abuse, using large-capacity lithium iron phosphate batteries as the subject of investigation. Through a combination of experimental simulation, an experimental platform for lithium-ion battery TR and a simulation model for lithium-ion battery TR are established, investigating the temperature characteristics and influencing factors during the battery's TR process. The subsequent sections of this paper are organized as follows. In Section 2, the TR experiments of lithium-ion batteries are conducted, and the obtained conclusions are presented. In Section 3, the TR model is developed and validated, and numerical results are provided and discussed. In Section 4, some conclusions are summarized.

## 2. Experimental Research of TR in Lithium Iron Phosphate Batteries

### 2.1. Experimental Setup and Methods

The experimental batteries utilized in this study were provided by Luoyang CALB (China Aviation Lithium Battery Co., Ltd., Luoyang, China). The batteries had dimensions of 173 mm × 54 mm × 207 mm and a rated capacity of 230 Ah. The charge and discharge cut-off voltages were set at 3.65 V and 2.5 V, respectively. The positive electrode material of the battery was lithium iron phosphate, while the negative electrode material was graphite. Details regarding the experimental battery samples and certain parameters can be found in Figure 1 and Table 1, respectively. Prior to the experiment, the sample batteries were charged at a constant current of 1 C to 3.65 V, followed by constant voltage charging at

3.65 V with a current of 0.05 C until reaching 100% state of charge (SOC). After completing the charging process, the experimental batteries were left to stabilize indoors for 24 h prior to conducting the TR experiments.

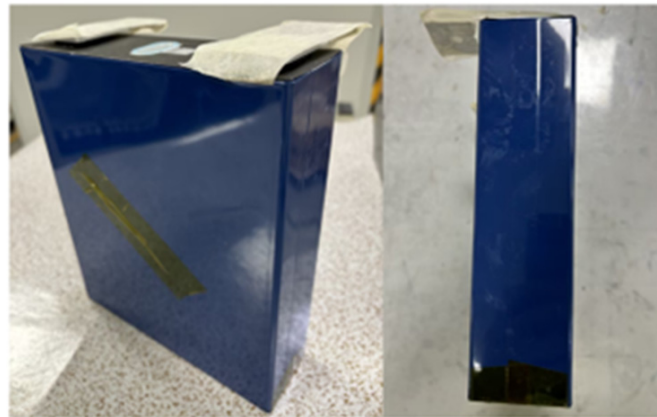


Figure 1. Battery physical diagram.

Table 1. The basic parameters of the lithium-ion battery.

Parameter	Numerical Value
Battery size	173 mm × 54 mm × 207 mm
Battery rated capacity	230 Ah
Nominal battery voltage	3.34 V
Battery charge/discharge cut-off voltage	2.5~3.65 V
Battery energy rating	170 Wh/kg
Battery mass	4185 ± 3 g

The experiments in this study were conducted within a safety laboratory. The experimental setup is illustrated in Figure 2. Thin-film thermocouples were utilized to measure the temperature during the experiment. Three temperature measurement points, labeled  $T_1$ ,  $T_2$ , and  $T_3$ , were positioned at the central regions of the front, back, and bottom surfaces of the battery, respectively. These thermocouples were employed to monitor and record the temperature variations occurring on the surface of the battery throughout the course of the experiment.

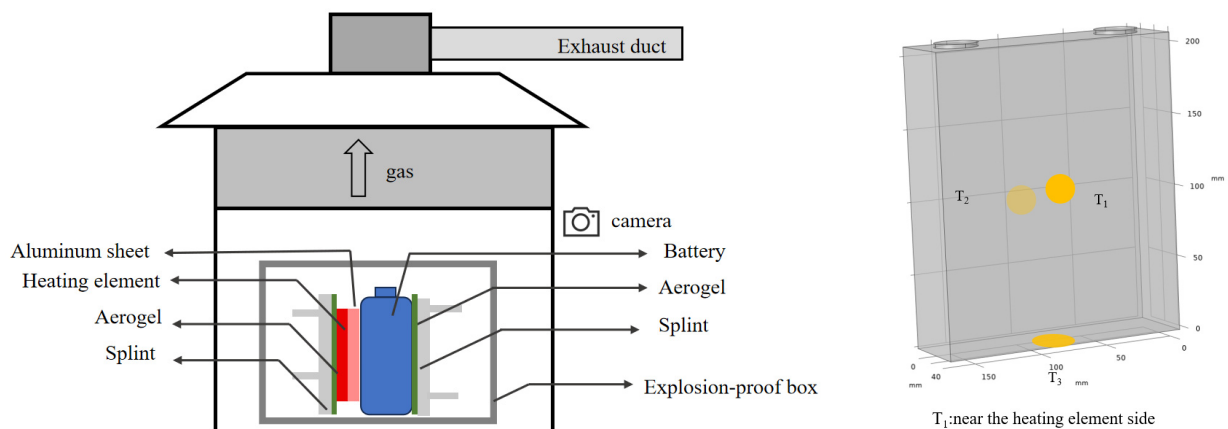


Figure 2. Schematic diagram of the battery TR experimental device.

During the experiment, TR in lithium-ion batteries was triggered by single-sided heating. The heating element was positioned at the center of the front side of the battery, which had dimensions of  $186 \text{ mm} \times 127 \text{ mm} \times 2 \text{ mm}$ . Four different heating powers were applied: 300 W, 500 W, 700 W, and 900 W. The initiation of heating was recorded as the start time of the experiment. According to the criteria for determining lithium-ion battery TR [35], the battery was considered to meet the TR standard when the temperature at the back surface of the battery reached its highest operating temperature and the temperature rise rate was  $\geq 1 \text{ }^\circ\text{C}$ , with a duration of at least 3 s. In such cases, the power was turned off, and the heating was ceased.

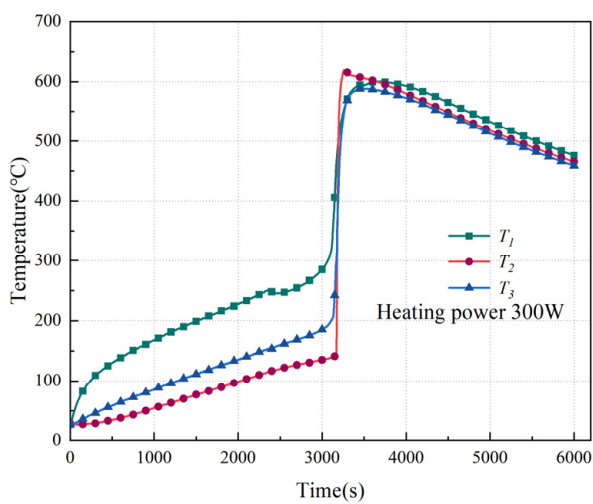
To ensure uniform heating of the entire surface of the battery, a 2 mm thick uniform heat aluminum plate was placed between the heating element and the battery. The size of the aluminum plate matched that of the heating element. Additionally, 3 mm thick aerogel pads were placed on the left side of the heating element and the right side of the battery to reduce heat dissipation during the TR process. During heating, the battery experienced significant expansion. To ensure good thermal contact between the battery and the uniform heat aluminum plate, two clamps were placed on the outermost sides and securely fastened with screws and nuts.

The assembled experimental setup was placed inside an explosion-proof box located in the safety laboratory. Power lines, temperature sensing wires, and other connecting cables were routed out from specific locations on the explosion-proof box and connected to the respective recorders. The ventilation system was activated to collect and treat the gases generated during the experiment to prevent environmental pollution. A camera was mounted above the safety laboratory to record the thermal runaway process. The battery was weighed before and after the TR experiment to measure the loss of mass during the experimental process.

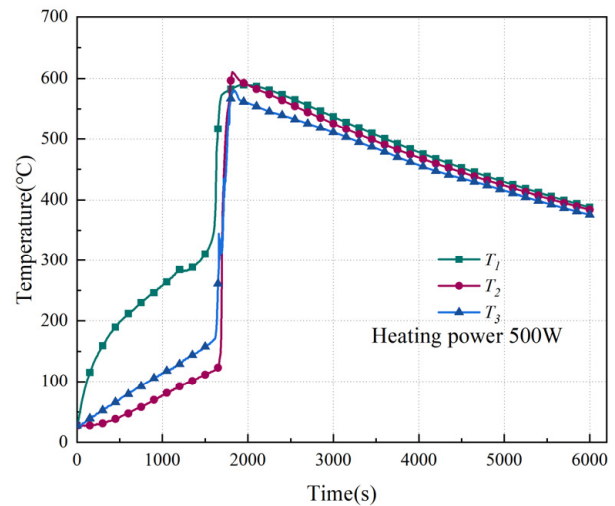
## 2.2. Analysis of Experimental Results

### 2.2.1. Variation of Battery Surface Temperature under Different Heating Power

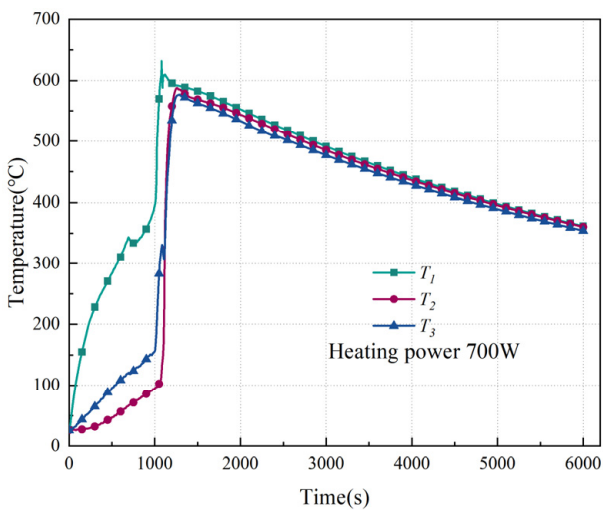
Different heating powers have been used to trigger TR in lithium-ion batteries, and the battery surface temperature is depicted in Figure 3. Upon activation of the heating plate, the temperature of the front surface ( $T_1$ ) exhibits a slow rise. Heat is then transferred from  $T_1$  towards the opposing side and bottom of the battery, subsequently causing the temperatures of the back surface ( $T_2$ ) and bottom surface ( $T_3$ ) to increase successively. As the experiment progresses, the temperature difference between  $T_3$  and  $T_2$  gradually widens. In the early stages of TR, the battery temperature experiences a gradual increase with relatively low internal heat generation. However, once the battery safety valve opens, the gas produced within the battery momentarily carries away some of the heat, resulting in a brief decrease in temperature. Following this stage, the internal separator of the battery undergoes shrinkage, leading to an internal short circuit. Consequently, there is a sharp rise in battery temperature, which marks the occurrence of TR. Within a very short period, intense exothermic reactions take place within the battery, releasing a substantial amount of heat. This, in turn, rapidly elevates the battery temperature. As the reaction progresses, internal substances are consumed, ultimately leading to the complete depletion of these substances. At this point, the battery temperature reaches its peak. Through the process of heat conduction, the heat generated inside the battery gradually transfers to its surface. The battery surface then engages in convective heat transfer with the surrounding environment, resulting in a gradual reduction in battery temperature. Furthermore, it is observed that the increase in heating power advances the reaction time of TR. Specifically, the triggering times of TR for heating powers of 300 W, 500 W, 700 W, and 900 W are 3106 s, 1550 s, 957 s, and 462 s, respectively.



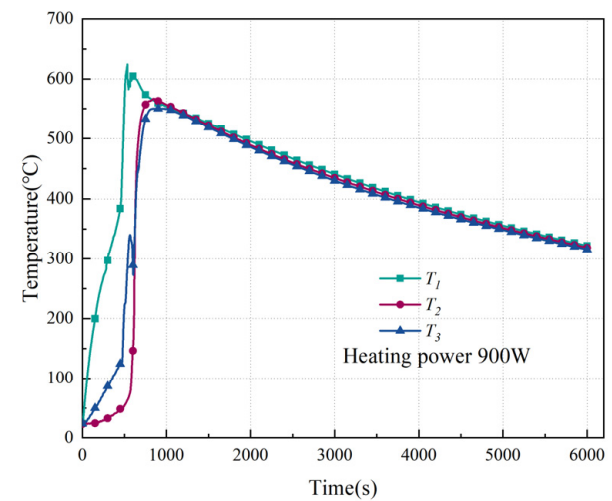
(a)



(b)



(c)



(d)

**Figure 3.** Variations of battery surface temperature under different heating powers. (a) Heating power 300 W; (b) heating power 500 W; (c) heating power 700 W; (d) heating power 900 W.

During the TR process of lithium-ion batteries, exothermic reactions generate significant heat, resulting in the production of a substantial amount of smoke within the battery. When the internal gas pressure of the battery reaches a specific threshold, the safety valve ruptures, leading to the release of a considerable quantity of white smoke and some electrolytes through the valve outlet. As TR continues, the amount of smoke generated gradually intensifies, ultimately filling the entire room. Consequently, visibility inside the room deteriorates close to zero. Figure 4 illustrates the TR process of lithium-ion batteries under a heating power of 300 W.

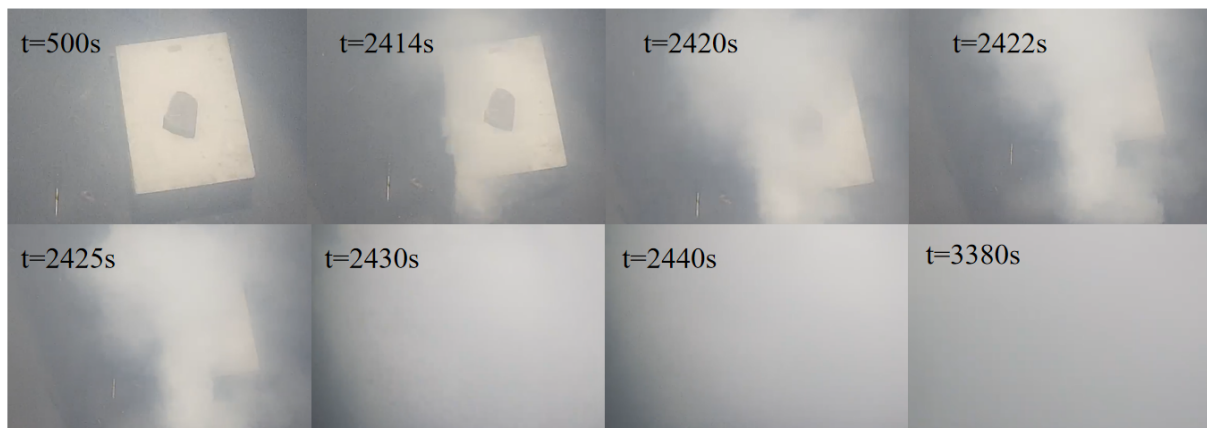


**Figure 4.** TR process of the lithium-ion battery under the heating power of 300 W.

### 2.2.2. Changes in Battery Mass and Thickness before and after TR

Figure 5a,b present the variations in mass and thickness of lithium-ion batteries before and after TR at different heating powers. The occurrence of TR in lithium-ion batteries leads to the generation of a substantial amount of smoke within the battery, causing an elevation in internal pressure. The smoke is compressed towards the sides, resulting in an increase in battery thickness. Once the internal smoke pressure reaches a specific threshold, the safety valve ruptures, leading to the release of a significant quantity of white smoke and electrolytes, consequently causing a reduction in battery mass. At heating powers of 300 W, 500 W, 700 W, and 900 W, the reduction in battery mass before and after TR is observed to be 849 g, 860 g, 859 g, and 852 g, respectively. Concurrently, the corresponding changes in battery thickness are measured as 4.04 mm, 6.27 mm, 4.08 mm, and 5.26 mm. Notably, the highest amount of gas and electrolyte expelled during TR is observed at a heating power of 500 W, which subsequently leads to the highest mass loss ratio (20.55%) and expansion rate (11.6%), as shown in Figure 6.

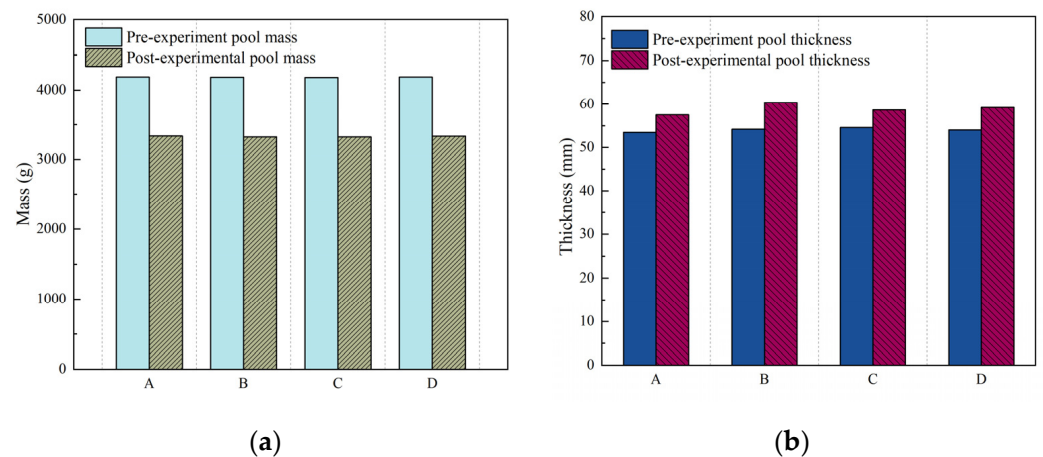


**Figure 5.** Changes in battery mass and thickness before and after thermal runaway. (a) Variation in battery mass; (b) variation in battery thickness. A: Heating power 300 W; B: heating power 500 W; C: heating power 700 W; D: heating power 900 W.

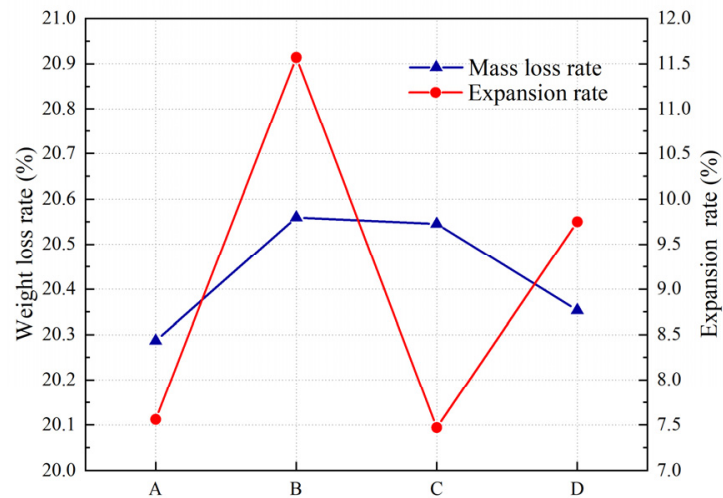


**Figure 6.** Battery mass loss ratio and expansion rate. A: Heating power 300 W; B: heating power 500 W; C: heating power 700 W; D: heating power 900 W.

### 3. Numerical Research of TR in Lithium Iron Phosphate Batteries

In order to gain a more detailed understanding of the heat generation distribution and temperature field prediction in lithium-ion batteries during TR, COMSOL Multiphysics 6.1 numerical simulation software was utilized. A simulation model was developed to investigate TR in lithium iron phosphate batteries, enabling the examination of temperature field distribution, changes in internal substance content, and heat generation distribution throughout the TR process of the battery.

#### 3.1. Mathematical Model

##### 3.1.1. Thermal Abuse Model

During the TR process of lithium-ion batteries, exothermic reactions occur inside the battery, releasing a large amount of heat in a very short time. There are four main exothermic reactions in the process: the solid electrolyte interface (SEI) decomposition reaction, negative-electrolyte reaction, positive-electrolyte reaction, and electrolyte decomposition reaction [36,37].

##### (1) SEI decomposition reaction

As the battery temperature reaches approximately 80 °C to 120 °C [10], the SEI membrane begins to undergo decomposition, generating heat that further elevates the battery's temperature. The decomposition reaction of the SEI membrane can be represented by the following chemical equation:

$$R_{sei} = A_{sei} \exp\left(-\frac{E_{a,sei}}{RT}\right) c_{sei}^{m,sei} \quad (1)$$

$$\frac{dc_{sei}}{dt} = -R_{sei} \quad (2)$$

$$Q_{sei} = H_{sei} \cdot W_{sei} \cdot R_{sei} \quad (3)$$

where the subscript *sei* represents the SEI decomposition reaction;  $R_{sei}$  is the rate of the SEI decomposition reaction,  $A$  is the pre-exponential factor of the reaction rate,  $E_a$  is the activation energy of the reaction,  $R$  is the gas constant for reactions, with a value of 8.314 J/(mol·K),  $T$  is the reaction temperature,  $c$  is the dimensionless amount of lithium-containing meta-stable species in the SEI,  $m$  is the reaction order,  $Q$  is the heat generated by the reaction,  $H$  is the specific enthalpy of reaction, and  $W$  is the mass of reactants.

## (2) Negative electrode–electrolyte reaction

When the temperature surpasses 120 °C [10], the process of lithium intercalation into the negative electrode initiates a reaction with the electrolyte. The decomposition reaction can be delineated by the following chemical equation:

$$R_{ne} = A_{ne} \exp\left(-\frac{t_{sei}}{t_{sei,ref}}\right) \exp\left(-\frac{E_{a,ne}}{RT}\right) c_{ne}^{m,ne} \quad (4)$$

$$\frac{dt_{sei}}{dt} = R_{ne} \quad (5)$$

$$\frac{dc_{ne}}{dt} = -R_{ne} \quad (6)$$

$$Q_{ne} = H_{ne} \cdot W_{ne} \cdot R_{ne} \quad (7)$$

where the subscript *ne* signifies the negative-electrolyte reaction and  $t_{sei}$  is the ratio of the thickness of the SEI membrane to the characteristic size of the active particles.  $t_{sei,ref}$  is the initial SEI membrane thickness to the characteristic size ratio of the active particles at the outset of the reaction.

## (3) Positive electrode–electrolyte reaction

The positive electrode undergoes an exothermic reaction with the electrolyte, resulting in the release of a significant amount of heat. Concurrently, the positive electrode material undergoes decomposition, yielding oxygen gas, which further contributes to the exothermic process upon reacting with the electrolyte. The decomposition reactions of the positive electrode and the electrolyte are represented by the following chemical equations:

$$R_{pe} = A_{pe} \alpha (1 - \alpha) \exp\left(-\frac{E_{a,pe}}{RT}\right) \quad (8)$$

$$\frac{d\alpha}{dt} = -R_{pe} \quad (9)$$

$$Q_{pe} = H_{pe} \cdot W_{pe} \cdot R_{pe} \quad (10)$$

where the subscript *pe* is the reaction occurring at the interface between the positive electrode and the electrolyte. The parameter  $\alpha$  is the dimensionless amount of lithium intercalated within the positive electrode, indicating the extent to which the positive electrode material undergoes transformation during the reaction.

## (4) Electrolyte Decomposition Reaction

When the temperature exceeds 200 °C [10], the electrolyte itself initiates decomposition reactions. The decomposition reaction of the electrolyte is represented by the following reaction equation:

$$R_{ele} = A_{ele} \exp\left(-\frac{E_{a,ele}}{RT}\right) c_{ele}^{m,ne} \quad (11)$$

$$\frac{dc_{ele}}{dt} = -R_{ele} \quad (12)$$

$$Q_{ele} = H_{ele} \cdot W_{ele} \cdot R_{ele} \quad (13)$$

where the subscript *ele* denotes the decomposition reaction of the electrolyte.

The total heat associated with the decomposition reactions during battery TR is given by

$$\sum Q_{tot} = Q_{sei} + Q_{ne} + Q_{pe} + Q_{ele} \quad (14)$$

### 3.1.2. Heat Transfer Model

During the TR process of lithium-ion batteries, heat exchange occurs between the battery and its surroundings, resulting in changes in the battery's own temperature. The heat transfer equations are given in references [38,39].

$$\rho c_p \frac{\partial T}{\partial t} + \nabla \cdot k \nabla T = Q_{tot} - A_0 h (T - T_0) \quad (15)$$

where  $\rho$  represents the average density of the battery;  $c_p$  is the average specific heat capacity of the battery;  $k$  is the thermal conductivity coefficient in various directions of the battery;  $h$  is the convective heat transfer coefficient; and  $A_0$  is the heat exchange area.

In this study, numerical simulation software was employed to conduct TR simulation analysis of lithium iron phosphate batteries. Certain simplifications were implemented to the model during the simulation process. It was assumed that the distribution of substances within the battery model was uniform and certain battery structural details were neglected. Additionally, effects such as flame, combustion, and the ejection of smoke particles on the simulation model were disregarded. Parameters involved in the simulation process were assumed to remain constant over time. Only convective heat transfer at the boundaries was considered, and only heat release from exothermic reactions was taken into account during TR, while polarization heat, Joule heat, and electrochemical heat were ignored [20,40]. The three-dimensional TR model of the battery is shown in Figure 7, and the thermal physical parameters of the battery are listed in Table 2. Based on the TR mechanism, a TR model for lithium-ion batteries was constructed, and exothermic reaction parameters were set according to the actual operating conditions of lithium-ion batteries, as shown in Table 3. The relevant parameters used in the modeling process were obtained from battery manufacturers, literature references [41–48], and fine-tuning based on comparison with experimental results.

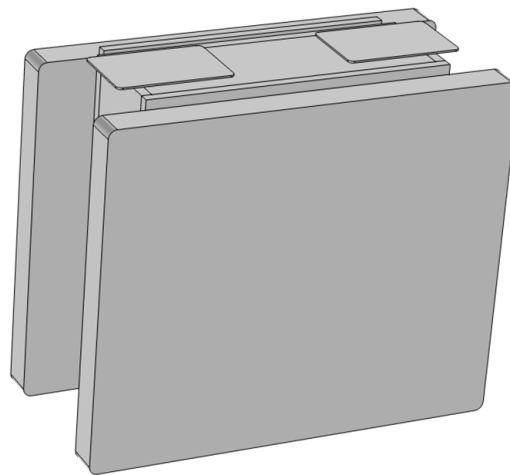


**Figure 7.** A 3D model of the lithium-ion battery.

**Table 2.** Thermal physical property parameters of the battery.

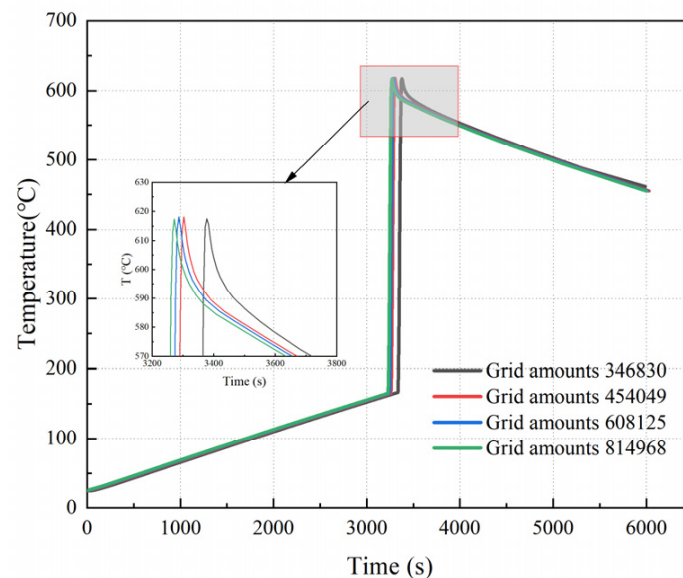
Parameter	Numerical Value
Average battery density	2151.2 kg/m <sup>3</sup>
Average battery-specific heat capacity	1412 J/(kg·K)
X-direction thermal conductivity coefficient	18 W/(m·K)
Y-direction thermal conductivity coefficient	1.5 W/(m·K)
Z-direction thermal conductivity coefficient	18 W/(m·K)

**Table 3.** Physical and kinetic parameters used for abuse simulations.

Parameter	SEI Decomposition Reaction	Negative Electrode–Electrolyte Reaction	Positive Electrode–Electrolyte Reaction	Electrolyte Decomposition Reaction
Specific enthalpy $H$	$7.2076 \times 10^5$ (J/kg)	$8.9957 \times 10^5$ (J/kg)	$2.527 \times 10^5$ (J/kg)	$1.6 \times 10^5$ (J/kg)
Mass of reactants $W$	413 (kg/m <sup>3</sup> )	413 (kg/m <sup>3</sup> )	925 (kg/m <sup>3</sup> )	500 (kg/m <sup>3</sup> )
Indexing factor $A$	$1.7 \times 10^{15}$ (s <sup>-1</sup> )	$2.5 \times 10^{13}$ (s <sup>-1</sup> )	$6.7 \times 10^{13}$ (s <sup>-1</sup> )	$5.14 \times 10^{25}$ (s <sup>-1</sup> )
Reaction activation energy (REA) $E_a$	$1.14005 \times 10^5$ (J/mol)	$1.16583 \times 10^5$ (J/mol)	$1.25983 \times 10^5$ (J/mol)	$2.7 \times 10^5$ (J/mol)

### 3.2. Model Validation and Grid Independence Verification

The accuracy of the simulation results in this study is closely related to the quality of the grid used. A higher grid accuracy leads to more accurate simulation results. For the TR model of lithium iron phosphate batteries, a tetrahedral mesh was employed overall, with local refinement in areas such as the cell, aluminum sheet, and heating element. In this study, four different grid densities were selected to compare the output results for battery back surface ( $T_2$ ) temperature triggered by a heating power of 300 W in order to determine the optimal number of grid divisions. The results, as shown in Figure 8, indicate that when the grid amounts are 368,274, there are slight differences compared to the results obtained with other grid quantities, while the differences in output results among the remaining three grid quantities are minimal. Considering the solution speed and computer memory usage, the optimal grid quantity was determined to be 454,049.

**Figure 8.** Comparison of results with different grid amounts.

The results of the simulation and experiment are compared and analyzed, as shown in Figure 9. The trend of simulation results matches well with that of the experiments. Initially, the temperature gradually increases until it reaches a certain threshold, at which point the diaphragm ruptures, triggering a rapid and intense reaction that releases significant heat. Consequently, the surface temperature of the battery rises sharply, reaches its peak, and then gradually decreases, as shown in Figure 10. There is some deviation between the simulation results and the experimental data, which could be attributed to the selection of certain parameters in the simulation process based on literature from the same battery type system, leading to slight discrepancies from the actual battery parameters. Additionally, environmental factors such as temperature and humidity during the experimental process may also contribute to differences between the measured and simulated results. However,

the temperature trends in the simulation results are similar to those in the experimental results, with an average error within 5%, indicating good agreement. The established TR model can effectively reflect the temperature characteristics of lithium iron phosphate batteries during the TR process.

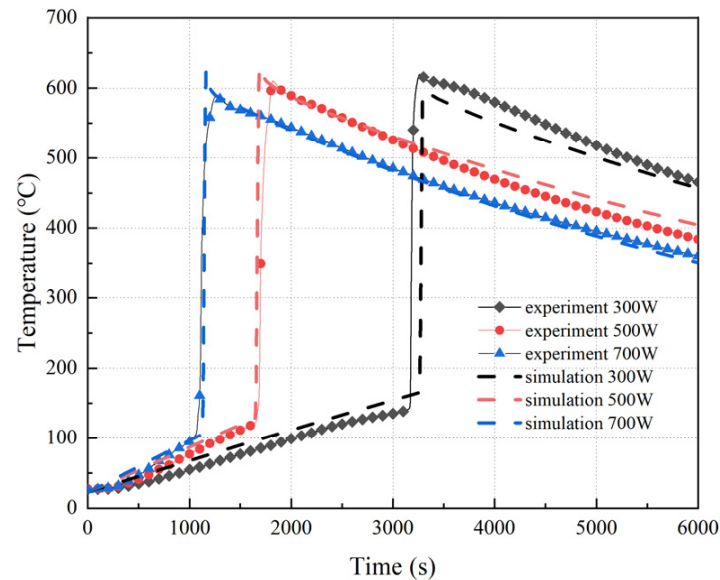


**Figure 9.** Comparison of simulation results with experimental results.

### 3.3. Analysis of Simulation Results

#### 3.3.1. Changes in Internal Substance Content during TR Processes

The changes in various substance components inside the battery under different heating powers are depicted in Figure 11. In the research process, a total of four variables were selected, namely,  $c_{sei}$ ,  $c_{ne}$ ,  $\alpha$ , and  $c_{ele}$ .  $c_{sei}$  is the dimensionless amount of lithium contained in the SEI,  $c_{ne}$  is the dimensionless amount of lithium intercalated within the negative electrode,  $\alpha$  is the dimensionless amount of lithium intercalated within the positive electrode, and  $c_{ele}$  is the dimensionless concentration of the electrolyte.

Upon applying a heating power of 300 W, the temperature of the battery exhibits a relatively slow rise during the initial stage (Stage I), as illustrated in Figure 12. Approximately at 1605 s, there is a gradual change in  $c_{sei}$  (Stage II), indicating the progressive decomposition of the SEI. Once the SEI decomposition reaches a certain extent, the lithium embedded in the negative electrode loses the protection of the SEI and starts to undergo decomposition reactions with the electrolyte, resulting in a significant decrease in  $c_{ne}$ , signifying the onset of an intense exothermic reaction stage (Stage III). Around 3390 s, reactions occur between the positive electrode and the electrolyte, leading to rapid changes in  $\alpha$ . Subsequently, the electrolyte begins to undergo decomposition reactions. During the time period from 3390 s to 3470 s,  $c_{ne}$ ,  $\alpha$ , and  $c_{ele}$  undergo rapid changes, indicating intense internal reactions in the battery. As the reactants are gradually consumed and the reactions reach a certain degree, the changes in the composition of various substances tend to stabilize (Stage IV).

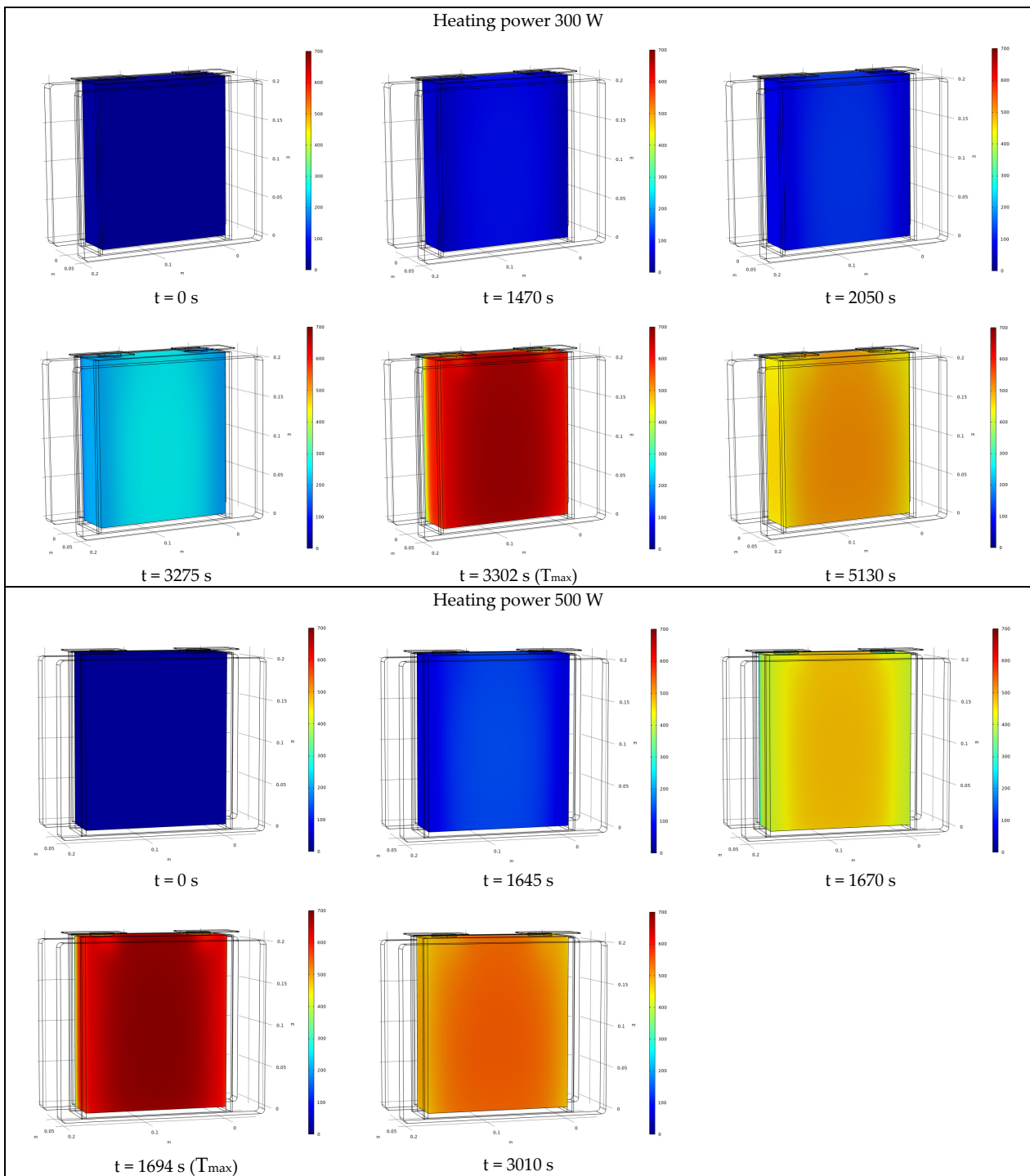


Figure 10. Cont.

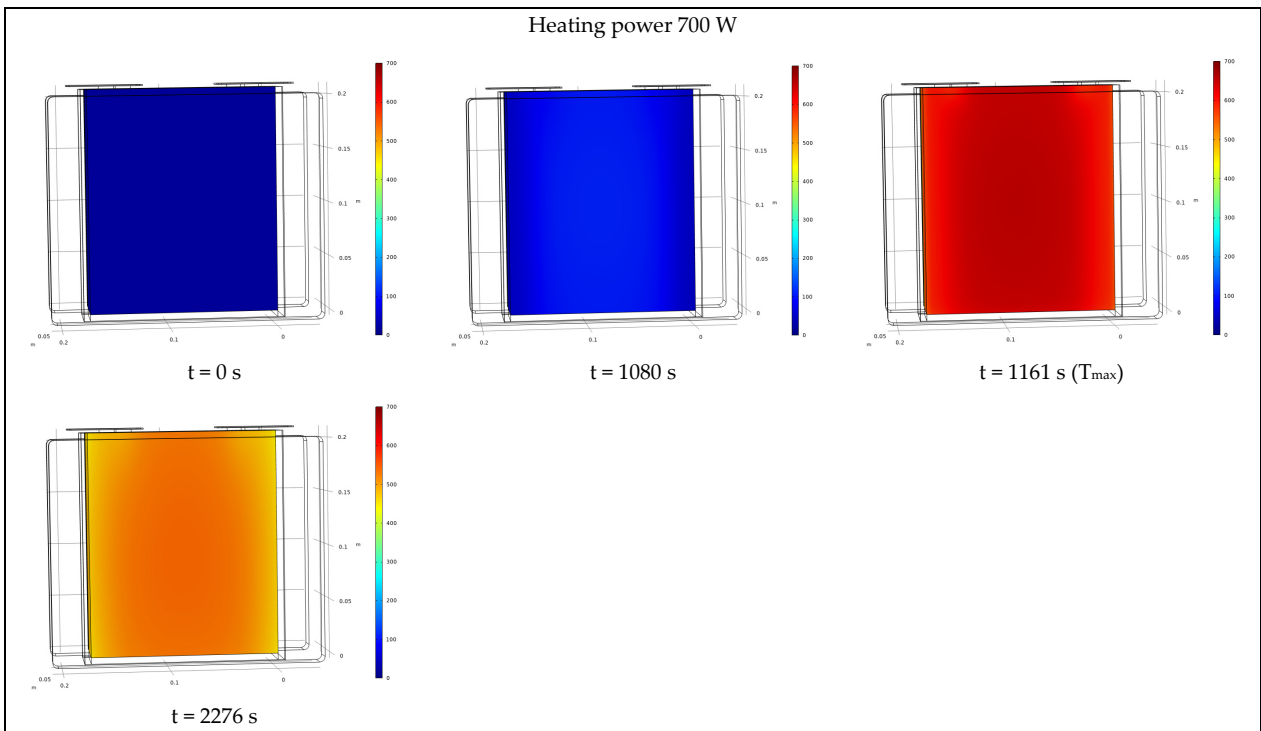


Figure 10. Temperature field distribution of the battery TR process.

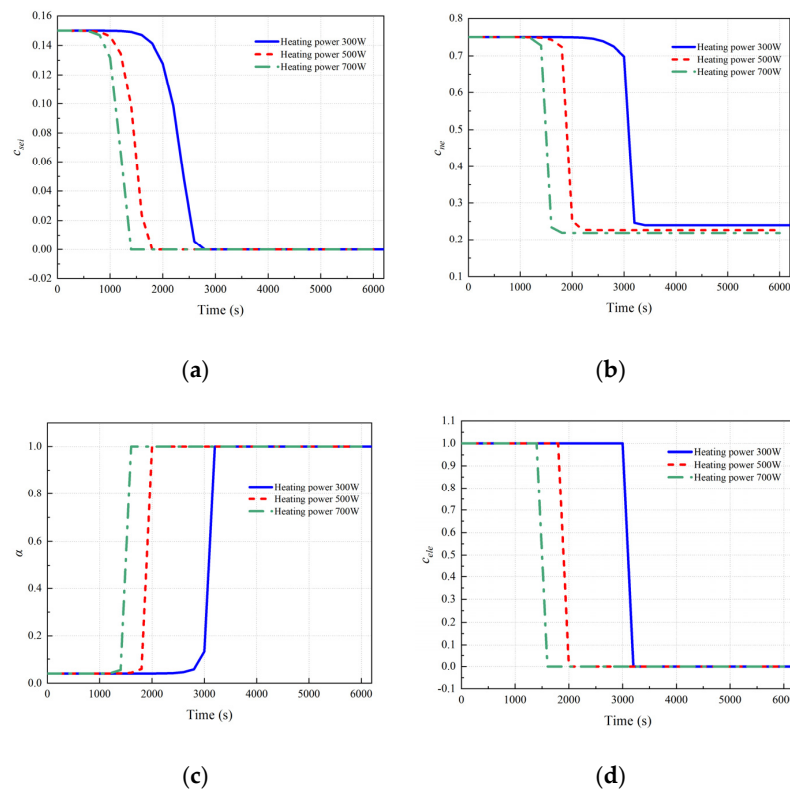
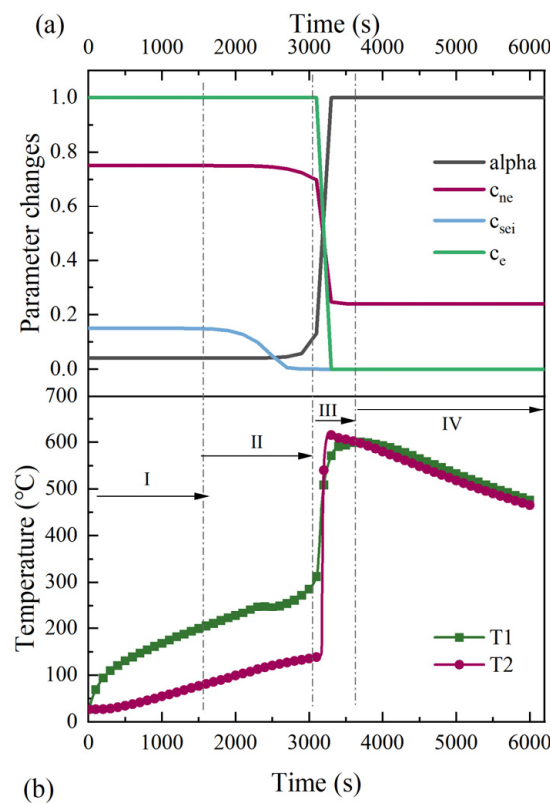


Figure 11. Internal substance content change in the lithium-ion battery. (a)  $c_{sei}$  is the dimensionless amount of lithium contained in the SEL, (b)  $c_{ne}$  is the dimensionless amount of lithium intercalated within the negative electrode, (c)  $\alpha$  is the dimensionless amount of lithium intercalated within the positive electrode, (d)  $c_{ele}$  is the dimensionless concentration of the electrolyte.



**Figure 12.** The corresponding graph of internal battery parameter changes with temperature. (a) Variations of internal substance content of the battery with heating power 300 W; (b) variation of the surface temperature of the battery with heating power 300 W.

As the heating power increases, the decomposition rate of the SEI decomposition accelerates, corresponding to an increased rate of change in  $c_{sei}$ . Compared to 300 W heating power, at 700 W heating power, the decomposition time of the SEI decomposition is advanced by approximately 830 s. The slopes of the  $\alpha$  and  $c_{ele}$  curves further increase, indicating a continuous acceleration in the reaction rates of the positive electrode and electrolyte. With the deepening of the reaction degree, the final steady-state value that  $c_{ne}$  can reach gradually decreases.

### 3.3.2. Analysis of Heat Generation Proportion during the TR Process

Figures 13 and 14 show the magnitude of heat production and the percentage of heat production of each side reaction inside the battery under the heating power of 300 W. Prior to the TR event in the battery, the SEI decomposition generates heat, which reaches the peak value of 77,865 KW/m<sup>3</sup> at 2590 s. Starting at 2300 s, the negative electrode–electrolyte reaction begins, initially exhibiting a low rate of heat production. However, after 3200 s, the heat production rate of the negative electrode–electrolyte reaction sharply increases. Concurrently, the positive electrode–electrolyte reaction and the decomposition reaction of the electrolyte itself occur, resulting in the release of a substantial amount of heat. These internal exothermic reactions intensify within the battery, causing the instantaneous conversion of electrical energy into internal energy. As a result, heat production rapidly escalates. Eventually, as the reactants are completely consumed, the heat production stabilizes.

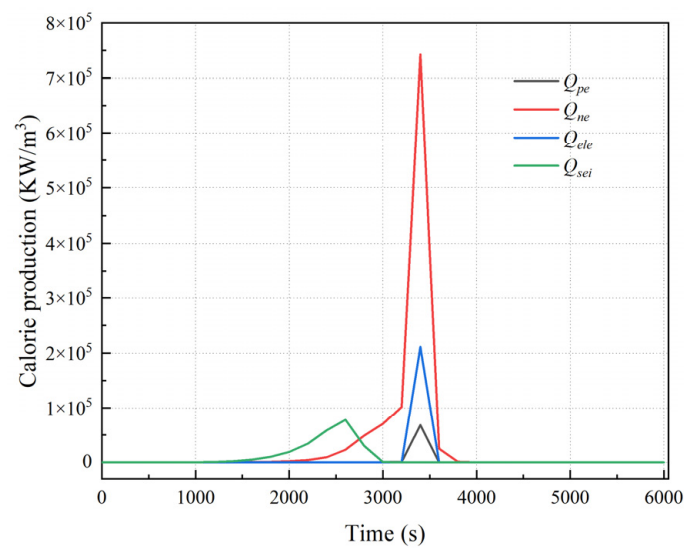


**Figure 13.** Battery TR heat production by each side reaction.

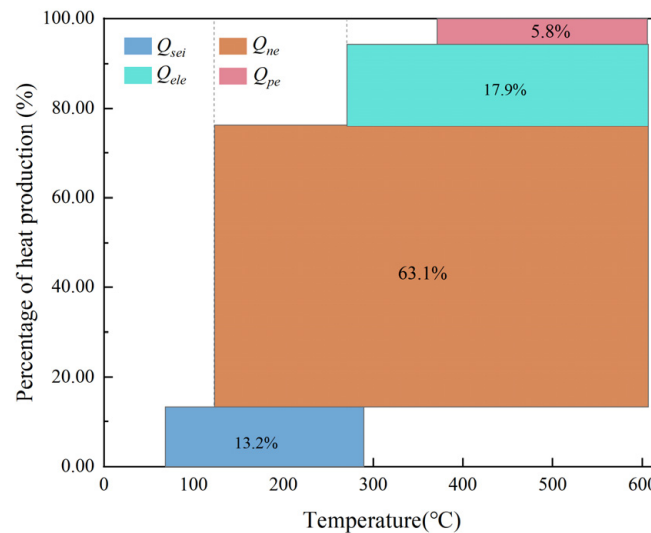


**Figure 14.** Percentage of heat produced by each side reaction of the TR battery.

The SEI decomposition reaction, negative electrode–electrolyte reaction, positive electrode–electrolyte reaction, and electrolyte decomposition reaction contribute 13.2%, 63.1%, 5.8%, and 17.9% to the total heat production, respectively. Among them, the negative electrode–electrolyte reaction accounts for the largest proportion of heat production, making it the primary source of heat throughout the entire process. This reaction is also responsible for the significant temperature change observed during the TR process of the battery.

### 3.3.3. Effects of the Heat Transfer Coefficient on TR

During the TR process of the battery, heat generated from internal chemical reactions is transferred to the battery surface. The battery surface then exchanges heat with the surrounding environment through convective heat transfer. In order to investigate the influence of the heat transfer coefficient on battery TR, simulations were conducted to analyze the temperature variation on the battery under a heating power of 300 W. The heat transfer coefficients considered in the simulations were 5 W/(m<sup>2</sup>·K), 10 W/(m<sup>2</sup>·K), 30 W/(m<sup>2</sup>·K), 50 W/(m<sup>2</sup>·K), 100 W/(m<sup>2</sup>·K), and 150 W/(m<sup>2</sup>·K).

The results, as shown in Figure 15, indicate that TR occurs in all cases when the heat transfer coefficients are  $5 \text{ W}/(\text{m}^2\cdot\text{K})$ ,  $10 \text{ W}/(\text{m}^2\cdot\text{K})$ ,  $30 \text{ W}/(\text{m}^2\cdot\text{K})$ , and  $50 \text{ W}/(\text{m}^2\cdot\text{K})$ . As the heat transfer coefficient increases, more heat is dissipated from the battery surface, resulting in a decrease in the peak temperature during TR and a delay in the occurrence of TR. When the heat transfer coefficient reaches  $100 \text{ W}/(\text{m}^2\cdot\text{K})$  and above, the heat generated by internal exothermic reactions in the battery can be efficiently transferred to the battery surface. This enables the battery surface to dissipate heat effectively through convective heat transfer, thus preventing the occurrence of TR. In practical production processes, it is recommended to select a suitable battery cooling method to mitigate the occurrence of TR to some extent.

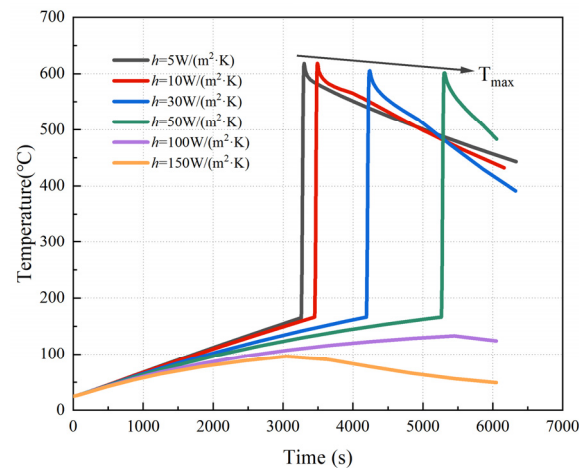


**Figure 15.** Variations of battery surface temperature under different heat transfer coefficients.

#### 4. Conclusions

This study conducted experimental and simulation analyses on high-capacity lithium iron phosphate batteries regarding TR. The experimental investigation focused on analyzing changes in battery surface temperature, mass, and expansion rate before and after TR, while the simulation study analyzed temperature variations during TR, changes in internal substance content, the rate of temperature rise of each component, heat generation patterns of various reactions, and the impact of heat transfer coefficients on lithium-ion battery TR. The following conclusions were drawn:

- (1) Batteries exhibit TR triggered by different heating powers, with an increase in heating power leading to a faster TR speed and deeper degrees of reaction for each component. However, the difference in peak temperature during TR is not significant.
- (2) Before and after TR, batteries undergo significant changes in mass and thickness. At a heating power of 500 W, the battery exhibits the highest mass loss ratio and expansion rate before and after TR, reaching 20.56% and 11.57%, respectively.
- (3) Simulation results indicate that during TR, the heat generation from the negative electrode–electrolyte reaction is the largest, accounting for 63.1% of the total heat release. Using high-temperature-resistant positive and negative electrode active materials can effectively delay or prevent lithium-ion battery TR.
- (4) The heat transfer coefficient is a crucial factor influencing battery TR. A higher heat transfer coefficient leads to faster temperature changes in the battery, delaying the occurrence of TR. When the heat transfer coefficient increases to  $100 \text{ W}/(\text{m}^2\cdot\text{K})$  or higher, the battery does not exhibit TR. Selecting an appropriate cooling method can, to some extent, prevent the occurrence of lithium-ion battery TR.

**Author Contributions:** Conceptualization, Q.Z., K.L. and X.Z.; methodology, Q.Z., K.L. and X.Z.; software, Q.Z.; validation, Q.Z.; data curation, Q.Z.; writing—original draft preparation, Q.Z.; writing—review and editing, Q.Z., K.L. and X.Z.; visualization, Q.Z.; supervision, K.L. and X.Z.; project administration, X.Z.; funding acquisition, K.L. All authors have read and agreed to the published version of the manuscript.

**Funding:** This research was funded by the Luoyang Science and Technology Development Plan Project, grant number [2302035A].

**Data Availability Statement:** The original contributions presented in the study are included in the article, further inquiries can be directed to the corresponding author.

**Conflicts of Interest:** The authors declare no conflicts of interest.

## Abbreviations

The following abbreviations are used in this manuscript:

$R_i$	The rate of the decomposition reaction
$A$	The pre-exponential factor of the reaction rate
$E_a$	The activation energy of the reaction
$R$	The gas constant for reactions, with a value of 8.314 J/(mol·K)
$T$	The reaction temperature
$c_{sei}$	The dimensionless amount of lithium contained in the SEI
$c_{ne}$	The dimensionless amount of lithium intercalated within the negative electrode
$c_{ele}$	The dimensionless concentration of the electrolyte
$m$	The reaction order
$Q$	Heat generated by the reaction
$H$	The heat of reaction per unit mass of reactant
$W$	The carbon content of the reactant
$t_{ref}$	The ratio of the thickness of the SEI membrane to the characteristic size of the active particles
$t_{sei,ref}$	The initial SEI membrane thickness to the characteristic size ratio of the active particles at the outset of the reaction
$\alpha$	The dimensionless amount of lithium intercalated within the positive electrode
$\rho$	The average density of the battery
$c_p$	The average specific heat capacity of the battery
$k$	The thermal conductivity coefficient in various directions of the battery
$h$	The convective heat transfer coefficient
$A_0$	The heat exchange area

## References

- Feng, X.; Ouyang, M.; Liu, X.; Lu, L.; Xia, Y.; He, X. Thermal runaway mechanism of lithium ion battery for electric vehicles: A review. *Energy Storage Mater.* **2018**, *10*, 246–267. [\[CrossRef\]](#)
- Choon, K.C.; Chi, H.; Jeyagopi, R. Optimizing Thermal Management System in Electric Vehicle Battery Packs for Sustainable Transportation. *Sustainability* **2023**, *15*, 11822. [\[CrossRef\]](#)
- Zhang, G.; Wei, X.; Tang, X.; Zhu, J.; Chen, S.; Dai, H. Internal short circuit mechanisms, experimental approaches and detection methods of lithium-ion batteries for electric vehicles: A review. *Renew. Sustain. Energy Rev.* **2021**, *141*, 110790. [\[CrossRef\]](#)
- Pugi, L.; Carlo, L.; Kociu, A.; Berzi, L.; Delohu, M. A Tool for Design and Simulation of Battery Operated Trains. In *Proceedings of the International Conference on Applications in Electronics Perovading Industry, Environment and Society*; Springer: Cham, Switzerland, 2023.
- Song, L.; Huang, Z.; Mei, W.; Jia, Z.; Yu, Y.; Wang, Q.; Jin, K. Thermal runaway propagation behavior and energy flow distribution analysis of 280 Ah LiFePO<sub>4</sub> battery. *Process. Saf. Environ.* **2023**, *170*, 1066–1078. [\[CrossRef\]](#)
- Lajunen, A.; Yang, Y.; Emadi, A. Review of Cabin Thermal Management for Electrified Passenger Vehicles. *IEEE Trans. Veh. Technol.* **2020**, *69*, 6025–6040. [\[CrossRef\]](#)
- Zhou, Z.; Li, M.; Zhou, X.; Li, L.; Ju, X.; Yang, L. Investigating thermal runaway triggering mechanism of the prismatic lithium iron phosphate battery under thermal abuse. *Renew. Energy* **2024**, *220*, 119674. [\[CrossRef\]](#)
- Wang, K.; Wu, D.; Chang, C.; Zhang, J.; Ouyang, D. Charging rate effect on overcharge-induced thermal runaway characteristics and gas venting behaviors for commercial lithium iron phosphate batteries. *J. Clean. Prod.* **2024**, *434*, 139992. [\[CrossRef\]](#)
- Huang, Z.; Yu, Y.; Duan, Q.; Qing, P. Heating position effect on internal thermal runaway propagation in large-format lithium iron phosphate battery. *Appl. Energy* **2022**, *325*, 119778. [\[CrossRef\]](#)
- Zhao, L.; Zhu, M.; Xu, X.; Gao, J. Thermal runaway characteristics on NCM lithium-ion batteries triggered by local heating under different heat dissipation conditions. *Appl. Therm. Eng.* **2019**, *159*, 113847.

11. Wang, Z.; Yuan, J.; Zhu, X.; Wang, H.; Huang, L.; Wang, Y.; Xu, S. Overcharge-to-thermal-runaway behavior and safety assessment of commercial lithium-ion cells with different cathode materials: A comparison study. *J. Energy Chem.* **2021**, *55*, 484–498. [[CrossRef](#)]
12. Feng, X.; Zheng, S.; Ren, D.; He, X.; Wang, L.; Cui, H.; Liu, X.; Hsu, H.; Gao, S.; Chen, T.; et al. Investigating the thermal runaway mechanisms of lithium-ion batteries based on thermal analysis database. *Appl. Energy* **2019**, *246*, 53–64. [[CrossRef](#)]
13. Feng, X.; Ren, D.; He, X.; Ouyang, M. Mitigating Thermal Runaway of Lithium-Ion Batteries. *Joule* **2020**, *4*, 743–770. [[CrossRef](#)]
14. Li, Z.; Zhang, P.; Shang, R. Effects of heating position on the thermal runaway propagation of a lithium-ion battery module in a battery enclosure. *Appl. Therm. Eng.* **2023**, *222*, 119830. [[CrossRef](#)]
15. Huang, P.; Yao, C.; Mao, B.; Wang, Q.; Sun, J.; Bai, Z. The critical characteristics and transition process of lithium-ion battery thermal runaway. *Energy* **2020**, *213*, 119082. [[CrossRef](#)]
16. Liu, P.; Li, S.; Jin, K.; Jin, K.; Fu, W.; Wang, C.; Jia, Z.; Jiang, L.; Wang, Q. Thermal Runaway and Fire Behaviors of Lithium Iron Phosphate Battery Induced by Overheating and Overcharging. *Fire Technol.* **2022**, *59*, 1051–1072. [[CrossRef](#)]
17. Ren, D.; Feng, X.; Lu, L.; Ouyang, M.; Zheng, S.; Li, J.; He, X. An electrochemical-thermal coupled overcharge to thermal-runaway model for lithium ion battery. *J. Power Sources* **2017**, *364*, 328–340. [[CrossRef](#)]
18. Ren, D.; Liu, X.; Feng, X.; Lu, L.; Ouyang, M.; Li, J.; He, X. Model-based thermal runaway prediction of lithium-ion batteries from kinetics analysis of cell components. *Appl. Energy* **2018**, *228*, 633–644. [[CrossRef](#)]
19. Ren, D.; Feng, X.; Liu, L.; Hus, H.; Lu, L.; Wang, L.; He, X.; Ouyang, M. Investigating the relationship between internal short circuit and thermal runaway of lithium-ion batteries under thermal abuse condition. *Energy Storage Mater.* **2021**, *34*, 563–573. [[CrossRef](#)]
20. Jin, C.; Sun, Y.; Wang, H.; Lai, X.; Wang, S.; Chen, S.; Rui, X.; Zheng, Y.; Feng, X.; Wang, H.; et al. Model and experiments to investigate thermal runaway characterization of lithium-ion batteries induced by external heating method. *J. Power Sources* **2021**, *504*, 230065. [[CrossRef](#)]
21. Zhang, Y.; Cheng, S.; Mei, W.; Jiang, L.; Zhuang, Z.; Cheng, Z.; Sun, J.; Wang, Q. Understanding of thermal runaway mechanism of LiFePO<sub>4</sub> battery in-depth by three-level analysis. *Appl. Energy* **2023**, *336*, 120695. [[CrossRef](#)]
22. Daniels, R.K.; Prabhakar, A. Experimental and numerical investigation on the effect of cell arrangement on thermal runaway propagation in air cooled cylindrical Li-ion battery modules. *J. Energy Storage* **2023**, *72*, 108191. [[CrossRef](#)]
23. Garcia, A.; Monsalve-serrano, J.; Lago, S.R. Numerical analysis of kinetic mechanisms for battery thermal runaway prediction in lithium-ion batteries. *Int. J. Engine Res.* **2021**, *23*, 1691–1707. [[CrossRef](#)]
24. Xu, C.; Wang, H.; Jiang, F.; Feng, X.; Lu, L.; Jin, C.; Zhang, F.; Huang, W.; Zhang, M.; Ouyang, M. Modelling of thermal runaway propagation in lithium-ion battery pack using reduced-order model. *Energy* **2023**, *268*, 126646. [[CrossRef](#)]
25. Jia, Z.; Wang, S.; Qin, P.; Li, C.; Song, L.; Cheng, Z.; Jin, K.; Sun, J.; Wang, Q. Comparative investigation of the thermal runaway and gas venting behaviors of large-format LiFePO<sub>4</sub> batteries caused by overcharging and overheating. *J. Energy Storage* **2023**, *61*, 106791. [[CrossRef](#)]
26. Koch, S.; Fill, A.; Birke, K.P. Comprehensive gas analysis on large scale automotive lithium-ion cells in thermal runaway. *J. Power Sources* **2018**, *398*, 106–112. [[CrossRef](#)]
27. Wang, S.; Song, L.; Li, C.; Tian, J.; Jin, K.; Duan, Q. Experimental study of gas production and flame behavior induced by the thermal runaway of 280 Ah lithium iron phosphate battery. *J. Energy Storage* **2023**, *74*, 109368. [[CrossRef](#)]
28. Huang, Z.; Zhao, C.; Li, H.; Peng, W.; Zhang, Z.; Wang, Q. Experimental study on thermal runaway and its propagation in the large format lithium ion battery module with two electrical connection modes. *Energy* **2020**, *205*, 117906. [[CrossRef](#)]
29. Yu, Y.; Huang, Z.; Mei, W.; Jia, Z.; Song, L.; Wang, Q. Preventing effect of different interstitial materials on thermal runaway propagation of large-format lithium iron phosphate battery module. *J. Energy Storage* **2023**, *63*, 107082. [[CrossRef](#)]
30. Xiao, Y.; Yan, M.; Shi, L.; Gong, L.; Cheng, X.; Zheng, H.; Pan, Y. High-temperature resistant, super elastic aerogel sheet prepared based on in-situ supercritical separation method for thermal runaway prohibition of lithium-ion batteries. *Energy Storage Mater.* **2023**, *61*, 102871. [[CrossRef](#)]
31. Huang, Z.; Liu, P.; Duan, Q.; Zhao, C.; Wang, Q. Experimental investigation on the cooling and suppression effects of liquid nitrogen on the thermal runaway of lithium ion battery. *J. Power Sources* **2021**, *495*, 229795. [[CrossRef](#)]
32. Li, Y.; Bai, M.; Zhou, Z.; Wu, W.; Lv, J.; Gao, L.; Huang, H.; Li, Y.; Song, Y. Experimental study of liquid immersion cooling for different cylindrical lithium-ion batteries under rapid charging conditions. *Therm. Sci. Eng. Prog.* **2023**, *37*, 101569. [[CrossRef](#)]
33. Li, Y.; Zhou, Z.; Hu, L.; Bai, M.; Hao, L.; Li, Y.; Liu, X.; Li, Y.; Song, Y. Experimental studies of liquid immersion cooling for 18650 lithium-ion battery under different discharging conditions. *Case Stud. Therm. Eng.* **2022**, *34*, 102034. [[CrossRef](#)]
34. Mallick, S.; Gayen, D. Thermal behaviour and thermal runaway propagation in lithium-ion battery systems—A critical review. *J. Energy Storage* **2023**, *62*, 106894. [[CrossRef](#)]
35. Shen, X.; Duan, Q.; Qin, P.; Wang, Q.; Sun, J. Experimental study on thermal runaway initiation and heat transfer characteristics of ternary lithium-ion batteries. *Energy Storage Sci. Technol.* **2023**, *12*, 1862–1871.
36. Zhang, Y.; Mei, W.; Qin, P.; Duan, Q.; Wang, Q. Numerical modeling on thermal runaway triggered by local overheating for lithium iron phosphate battery. *Appl. Therm. Eng.* **2021**, *192*, 116928. [[CrossRef](#)]
37. Liu, J.; Wang, Z.; Bai, J.; Gao, T.; Mao, N. Heat generation and thermal runaway mechanisms induced by overcharging of aged lithium-ion battery. *Appl. Therm. Eng.* **2022**, *212*, 118565. [[CrossRef](#)]

38. He, T.; Zhang, T.; Gadkari, S.; Wang, Z.; Mao, N.; Cai, Q. An investigation on thermal runaway behaviour of a cylindrical lithium-ion battery under different states of charge based on thermal tests and a three-dimensional thermal runaway model. *J. Clean. Prod.* **2023**, *388*, 135980. [[CrossRef](#)]
39. Lin, S.; Ling, Z.; Li, S.; Cai, C.; Zhang, Z.; Fang, X. Mitigation of lithium-ion battery thermal runaway and inhibition of thermal runaway propagation using inorganic salt hydrate with integrated latent heat and thermochemical storage. *Energy* **2023**, *266*, 126481. [[CrossRef](#)]
40. Lyu, P.; Liu, X.; Liu, C.; Zao, Z. The influence of tab overheating on thermal runaway propagation of pouch-type lithium-ion battery module with different tab connections. *Int. J. Heat Mass Trans.* **2023**, *211*, 124279. [[CrossRef](#)]
41. Kouiu, A.; Pugi, L.; Berzi, L.; Zacchini, E.; Delogu, M.; Baldanzini, N. Electrochemical and Thermal Modelling of a Li-Ion NMC Pouch Cell. In *Proceedings of the International Conference on Applications in Electronics Perovading Industry, Environment and Society*; Springer: Cham, Switzerland, 2023.
42. Ostanek, J.K.; Li, W.; Mukherjee, P.P.; Crompton, K.; Hacker, C. Simulating onset and evolution of thermal runaway in Li-ion cells using a coupled thermal and venting model. *Appl. Energy* **2020**, *268*, 114972. [[CrossRef](#)]
43. Song, L.; Wang, S.; Jia, Z.; Li, C.; Li, Y.; Cheng, Y.; Zhang, Y.; Yu, Y.; Jin, K.; Duan, Q. A comprehensive investigation of thermal runaway critical temperature and energy for lithium iron phosphate batteries. *J. Energy Storage* **2024**, *86*, 111162. [[CrossRef](#)]
44. Feng, X.; He, X.; Ouyang, M.; Lu, L.; Wu, P.; Kulp, C.; Prasser, S. Thermal runaway propagation model for designing a safer battery pack with 25 Ah LiNixCoyMnzO2 large format lithium ion battery. *Appl. Energy* **2015**, *154*, 74–91. [[CrossRef](#)]
45. Peng, P.; Jiang, F. Thermal safety of lithium-ion batteries with various cathode materials: A numerical study. *Int. J. Heat Mass Trans.* **2016**, *103*, 1008–1016. [[CrossRef](#)]
46. Kwak, E.; Kim, J.H.; Hong, S.H.; Oh, K. Detailed modeling investigation of thermal runaway pathways of a lithium iron phosphate battery. *Int. J. Energy Res.* **2022**, *46*, 1146–1167. [[CrossRef](#)]
47. Bugryniec, P.J.; Davidson, J.N.; Brown, S.F. Computational modelling of thermal runaway propagation potential in lithium iron phosphate battery packs. *Energy Rep.* **2020**, *6*, 189–197. [[CrossRef](#)]
48. Jin, C.; Sun, Y.; Wang, H.; Zheng, Y.; Wang, S.; Rui, X.; Xu, C.; Feng, X.; Wang, H.; Ouyang, M. Heating power and heating energy effect on the thermal runaway propagation characteristics of lithium-ion battery module: Experiments and modeling. *Appl. Energy* **2022**, *312*, 118760. [[CrossRef](#)]

**Disclaimer/Publisher's Note:** The statements, opinions and data contained in all publications are solely those of the individual author(s) and contributor(s) and not of MDPI and/or the editor(s). MDPI and/or the editor(s) disclaim responsibility for any injury to people or property resulting from any ideas, methods, instructions or products referred to in the content.